

Gapless electronic topology without free-electron counterpart

Haoyu Hu¹, Lei Chen¹, Chandan Setty¹, Sarah E. Grefe², Andrey Prokofiev³,
Stefan Kirchner^{4,5}, Silke Paschen^{3,1}, Jennifer Cano^{6,7}, and Qimiao Si^{1,*}

¹*Department of Physics and Astronomy, Rice Center for Quantum Materials, Rice University, Houston, Texas, 77005, USA*

²*Theoretical Division, Los Alamos National Laboratory, Los Alamos, New Mexico 87545, USA*

³*Institute of Solid State Physics, TU Wien, Wiedner Hauptstr. 8-10, 1040 Vienna, Austria*

⁴*Zhejiang Institute of Modern Physics, Zhejiang University, Hangzhou, Zhejiang 310058, China*

⁵*Zhejiang Province Key Laboratory of Quantum Technology and Devices, Zhejiang University, Hangzhou 310027, China*

⁶*Department of Physics and Astronomy, Stony Brook University, Stony Brook, NY 11794, USA*

⁷*Center for Computational Quantum Physics, Flatiron Institute, New York, NY 10010, USA*

The interplay between interactions and topology in quantum materials is of extensive current interest. For the gapless case, whether and how electron correlations can drive topological states that are not adiabatically connected to a noninteracting system is an open and pressing problem. Here we study a periodic Anderson model in several lattices, with strongly correlated electrons coupled to two channels of conduction electrons. Strong correlations are demonstrated to cooperate with lattice symmetry to produce topological phases that have no Landau quasi-particles and show strange-metal behavior. We characterize the electronic topology in terms of surface states and valley and spin Hall conductivities, and identify candidate materials to realize the proposed phases. Our work opens a door to a variety of gapless topological phases without free-electron counterpart in a broad range of strongly correlated metals.

States of matter and their transitions have traditionally been classified in terms of Landau's order-parameter paradigm, which is based on global symmetry and its spontaneous breaking (1). For free-electron systems, typically with large spin-orbit couplings, the topological paradigm classifies electronic states in terms of certain topological invariants associated with their quantum-mechanical wavefunctions (2). The electronic topology is responsible for various novel phenomena, such as unusual Hall effects and charge polarization. In recent years, there has been much progress made in realizing gapless topological phases, including those that harbor Weyl and Dirac fermions (3, 4). In classifying such topological semimetals, crystalline symmetries play a key role (5–10).

The importance of electron-electron interactions has been increasingly recognized in topological semimetals. Typically, one treats the perturbative effect of correlations on free-electron topological semimetals (3, 4). There has been considerable effort in pursuing strongly correlated topological semimetals (11, 12). In particular, recent work has demonstrated that correlations drive composite fermions with highly renormalized topological nodal excitations that are pinned to the Fermi energy, both theoretically (13, 14) and experimentally (15, 16). As exemplified by the fractional quantum Hall effect (17), strong correlations can lead to topological states that go beyond the noninteracting description; they possess new excitations with quantum numbers such as fractional charge. In the gapless case, no such topological systems have been known.

Here we advance the notion that electron fractionalization, driven by strong correlations, cooperate with space group symmetry constraints to produce gapless topological states that have no free-electron counterpart. To this end, we push a recently proposed design principle (18) to the extreme limit where Landau's quasiparticle concept breaks down. Figure 1A illustrates the idea that symmetry imposes constraints on emergent low energy excitations in such a regime, leading to strange-metallic topological phases. We provide a proof-of-principle demonstration of this idea in a well-defined model and propose strongly correlated materials to realize the new

topological phases.

We consider a periodic Anderson model, in which strongly correlated electrons act as local moments that are coupled to two degenerate channels of conduction electrons. While such a model can be considered in a generic setting for correlation physics (19), we focus on two representative lattices in which crystalline symmetries promote Dirac and Weyl nodes. The central ingredients of the model are electronic orbitals with strong Coulomb repulsion. As illustrated in Figure 1B, the interactions render these electrons as an effective local moment in the lowest energies, as denoted by a lowest doublet with (pseudo-)spins $\sigma = \uparrow, \downarrow$. This correlated local object hybridizes with two channels (see below and Supplementary Materials) of conduction electrons, labeled by $\alpha = 1, 2$; the hybridization involves the change of local electron number by 1, which turns the local configuration to $|\alpha = 1, 2\rangle$, and likewise from $|\alpha\rangle$ to $|\sigma\rangle$. The single-impurity version of this model, the two-channel Anderson/Kondo model, is well established to have non-Fermi liquid behavior (20–24); the electron correlations fractionalize the d -electron, leading to an emergent Majorana fermion (25, 26).

We start from the case of two-dimensional (2D) kagome lattice, and express the model in terms of the following Hamiltonian:

$$\begin{aligned}
H = & \sum_{ij,\sigma,\alpha} (t_{ij} - \mu\delta_{ij}) c_{i,\sigma,\alpha}^\dagger c_{j,\sigma,\alpha} \\
& + P \left[\epsilon_f \sum_{i,\sigma,\alpha} d_{i,\sigma,\alpha}^\dagger d_{i,\sigma,\alpha} + V \sum_{i,\sigma,\alpha} (c_{i,\sigma,\alpha}^\dagger d_{i,\sigma,\alpha} + \text{h.c.}) \right] P. \quad (1)
\end{aligned}$$

Here, $c_{i,\sigma,\alpha}$ ($d_{i,\sigma,\alpha}$) denotes a conduction (local) electron of spin σ and channel α on site i , which marks both the unit cell position and sub-lattice index. The projection operator P allows for the strongly correlated d -electrons to have two empty states $|1\rangle, |2\rangle$ and two singly occupied states $|\uparrow\rangle, |\downarrow\rangle$ at every site. In addition, t_{ij} is the hopping matrix of the conduction electrons, with μ acting as the chemical potential; ϵ_f specifies the spacing of the d -electron levels (Figure 1B), and V is the hybridization strength between the two types of electrons. We solve the model within

dynamical mean-field theory (DMFT) (27). The Green's function of conduction electrons are calculated via $G_c(\omega, \mathbf{k}) = [\omega - t_{\mathbf{k}} - \Sigma_c(\omega)]^{-1}$. Here, $t_{\mathbf{k}}$ is the hopping matrix in momentum space; $\Sigma_c(\omega)$ is the local self-energy which encodes all correlation effects driven by the multi-channel Kondo effect. We solve the dynamical equations in real frequency and reach extremely low temperatures – down to roughly 10^{-5} of the Kondo temperature (T_K) – in order to reveal the asymptotic low-energy behavior.

The imaginary part of the self-energy is found to depend on frequency in a square-root fashion in the low-energy limit, as shown in Figure 2A. This is in contrast to interacting systems that are described by Landau's quasiparticles, in which case $\text{Im}\Sigma_c(\omega)$ goes quadratically in ω . The square-root frequency dependence of the self-energy describes a strange metal, as characterized by an electrical resistivity that depends on temperature (T) in a \sqrt{T} way, as shown in Figure 2B. In practice, we find that the asymptotic behavior, in both the frequency and temperature dependences, appears only at sufficiently low temperatures; it was not found in previous DMFT solutions of the multichannel Kondo lattice model on the cubic lattice (28) solved at much higher temperatures (about $0.1 T_K$ and above). Our result is consistent with the expectation from the solutions to the corresponding single-impurity two-channel Kondo model (23). The asymptotic form of the self-energy, however, is not adequate for our purpose; on its own, it would not lead to new dispersive modes.

We find that the self-energy also contains a pole in the complex energy plane, as prescribed by Eq. 6 [see Supplementary Materials]. To our knowledge, this result is new; it is made possible by our working on the real-frequency axis and solving the problem at very low temperatures. The structure of the self-energy implies that, in spite of the absence of Landau quasiparticles, dispersive modes, which are characterized by the eigenvalues and eigenvectors of the Green's function [see Supplementary Materials], develop in the spectral function. For the kagome lattice, this is shown in Figure 3A. The dispersive modes are not quasiparticles. Indeed, for a given

wavevector \mathbf{k} , the spectral function vs. energy has peaks that, unlike the quasiparticle case, are not sharp: the width is always larger than the peak energy as measured from the Fermi energy. The dispersive modes capture the development of the correlated d -electron spectral weight in the immediate vicinity of the Fermi energy: they appear within a range of the Kondo energy.

What is remarkable is that these dispersive modes form Dirac nodes that appear in the immediate vicinity of the Fermi energy, as seen in Figure 3A. They form two close-by branches, which are illustrated more clearly in Figure 3B and Figure 3C, respectively. To understand the Dirac nodes, we analyze the structure of the interacting Green's function in terms of the Green's function eigenvectors and eigenfunctions (Supplementary Materials). An eigenvector specifies a dispersive mode, and the imaginary part of the corresponding eigenfunction describes its spectral function. The eigenvectors are labeled by the wavevector \mathbf{k} , and are subject to the same crystalline symmetry constraints as Bloch functions. Correspondingly, at the K (and K') points of the kagome lattice's Brillouin zone, symmetry dictates the double degeneracy of the dispersive modes (Supplementary Materials). In other words, a robust mechanism underlies the emergence of the Dirac nodes and the associated nodal excitations that go beyond Landau quasiparticles.

We next consider the three-dimensional (3D) kagome lattice, which corresponds to the stacking of the kagome planes with an added ingredient – the breaking of the inversion symmetry (Supplementary Materials). The conduction-electron self-energy behaves similarly as in the 2D case (see Figure S4B,E, Supplementary Materials). However, here the space-group symmetry – in particular, a C_{3z} symmetry – protects Weyl nodes (Supplementary Materials). Correspondingly, we find dispersive modes with non-Fermi liquid Weyl nodes, as shown in Figure 3D along the K - H line. The two adjacent dispersive branches are presented in Figure 3E and Figure 3F. In addition, there is another pair of Weyl nodes on the $-H$ - K' - H' line and a pair of Dirac nodes on $-A$ - Γ - A with similar spectral features.

The 3D case is particularly convenient to characterize the topological nature of these non-Fermi liquid nodes. We show spectral functions of surface states in Figure 4A; their exponential decay from the surface to the interior of the system is demonstrated in Supplementary Materials (Figure S5A). In addition, we have calculated the in-plane spin-Hall conductivity as a function of k_z . As shown in Figure 4B, it provides yet another characterization of the topological nature of the Weyl nodes.

The overall spin-Hall conductivity has a \sqrt{T} dependence, as shown in Figure 4C. Finally, we have calculated the nonlinear Hall effect, which displays a singular $\frac{1}{\sqrt{T}}$ dependence (Supplementary Materials, Sect. G). For the 2D Dirac case, we have calculated the valley Hall conductivity (see Supplementary Materials, Figure S6B). Its temperature dependence also displays a \sqrt{T} dependence, as seen in Figure 4C. The surface states and the various Hall effects noted above not only characterize the gapless topological phases, but also allow to identify them experimentally.

Having advanced genuinely interacting Dirac and Weyl semimetal phases, we now turn to their realization in strongly correlated materials. So far we have focused our analysis of the two-channel Anderson lattice on the 2D and 3D kagome lattices, by assuming the existence of the pertinent local degrees of freedom as illustrated in Figure 1B. From the model studies, we gain the key insight that the form of the electron self-energy, Eq. 6, is insensitive to the underlying lattice, provided the required local degrees of freedom are in place; for example, we have shown that it has essentially the same form not only in the 2D kagome lattice and the noncentrosymmetric 3D kagome lattice but also in the cubic lattice (see Figure S4C, F, Supplementary Materials). This equation encodes the two-channel nature of the Anderson or Kondo lattice. We thus look for space group symmetries that constrain nodes in the dispersion while also allowing for the local degrees of freedom of Figure 1B.

This prescription has led us to three materials, the centrosymmetric PrBi (29,30) and PrFe₄P₁₂

(31, 32), as well as the noncentrosymmetric UPt_3Au_2 (33), with the space groups #225, #204, and #216, respectively, and the point group symmetries O_h , T_h , and T_d at the Pr/U site. The Pr^{3+} and U^{4+} ions have the electronic configuration $4f^2$ which, for these point group symmetries, *can* lead to a Γ_3 non-Kramers doublet ground state. A non-Kramers doublet can be treated as pseudo-spin degree of freedom. The first excited levels are then Kramers doublets, whose spin degrees of freedom provide the pseudo-channel index (22). PrBi has a low charge carrier concentration (30), $\text{PrFe}_4\text{P}_{12}$ can be readily tuned to such a state (31), and UPt_3Au_2 (33) exhibits a very weakly temperature-dependent resistivity, all suggestive of semimetallic ground states (see Supplementary Materials, Sect. H for further details). Analysis of space group symmetry constraints suggests the emergence of symmetry protected Dirac nodes in PrBi and $\text{PrFe}_4\text{P}_{12}$ and symmetry protected Weyl nodes in UPt_3Au_2 (see Supplementary Materials, Sect. I). We thus put forward the three as candidate materials to realize the proposed gapless correlated topological phases.

We close with two pertinent remarks. One concerns the additional low-energy physics that the beyond-free-electron topological semimetals may harbor. An emerging paradigm in strongly correlated systems is that strange metals nucleate novel phases. For generic lattices, multi-channel local correlations may lead to broken-symmetry phases such as superconductivity (34), multipolar order (35) or even channel-symmetry-broken “hastatic” order (19). It will be instructive to explore whether these and other types of ordered states develop from the topological semimetal phases we have advanced, and any new physics that the nontrivial topology brings in these states.

More generally, our findings provide an extreme case of a general design principle recently advanced (18), *viz.* space group symmetry constrains collective excitations that emerge from strong correlations. The two-channel Kondo effect places the correlation physics in the regime of electron fractionalization. Even so, the space group symmetry acts on the eigenvectors of the

single-particle Green's functions and provides a robust route to topological semimetals, albeit ones that cannot be adiabatically connected to free-electron systems.

To summarize, our work has advanced the first examples of topological semimetals that have no free-electron counterpart. Utilizing a centrosymmetric lattice in two dimensions and a non-centrosymmetric lattice in three dimensions, we have shown how their space group symmetries cooperate with the correlation physics of the two-channel Kondo effect to produce Dirac and Weyl nodes near the Fermi energy without Landau quasiparticles. Guided by the considerations of both symmetry and strong correlations, we have proposed several materials to realize these strongly correlated topological semimetals. It is anticipated that the proposed route will lead to the uncovering of gapless topological phases without free-electron counterpart in a variety of other strongly correlated materials and structures.

Acknowledgments: Work at Rice has been supported by the the National Science Foundation under Grant No. DMR-1920740 (L.C. and Q.S.), the Air Force Office of Scientific Research under Grant No. FA9550-21-1-0356 (C.S.) and the Robert A. Welch Foundation Grant No. C-1411 (H.H.). The majority of the computational calculations have been performed on the Shared University Grid at Rice funded by NSF under Grant EIA-0216467, a partnership between Rice University, Sun Microsystems, and Sigma Solutions, Inc., the Big-Data Private-Cloud Research Cyberinfrastructure MRI-award funded by NSF under Grant No. CNS-1338099, and the Extreme Science and Engineering Discovery Environment (XSEDE) by NSF under Grant No. DMR170109. Work at Los Alamos was carried out under the auspices of the U.S. Department of Energy (DOE) National Nuclear Security Administration under Contract No. 89233218CNA000001, and was supported by LANL LDRD Program. A.P. and S.P. acknowledge funding from the Austrian Science Fund (projects No. I4047 and 29279) and the European Microkelvin Platform (H2020 project No. 824109). S.K. was in part supported by the National Key R&D Program of the MOST of China, Grant No. 2016YFA0300202 and the

National Science Foundation of China, Grant No. 11774307. J.C. acknowledges the support of the National Science Foundation under Grant No. DMR-1942447 and the support of the Flatiron Institute, a division of the Simons Foundation. Four of us (S.G., S.P., J.C. and Q.S.) acknowledge the hospitality of the Aspen Center for Physics, which is supported by NSF grant No. PHY-1607611.

Authors contributions: All authors contributed to the research of the work and the writing of the paper.

Competing interests: The authors have no competing interests.

Data availability: The data that support the findings of this study are available from the corresponding author upon reasonable request.

References

1. L. Landau, *Nature* **138**, 840 (1936).
2. D. Xiao, M.-C. Chang, Q. Niu, *Rev. Mod. Phys.* **82**, 1959 (2010).
3. N. P. Armitage, E. J. Mele, A. Vishwanath, *Rev. Mod. Phys.* **90**, 015001 (2018).
4. N. Nagaosa, T. Morimoto, Y. Tokura, *Nature Reviews Materials* **5**, 621 (2020).
5. B. Bradlyn, *et al.*, *Nature* **547**, 298 (2017).
6. J. Cano, *et al.*, *Phys. Rev. B* **97**, 035139 (2018).
7. H. C. Po, A. Vishwanath, H. Watanabe, *Nature Communications* **8**, 50 (2017).
8. H. Watanabe, H. C. Po, M. P. Zaletel, A. Vishwanath, *Phys. Rev. Lett.* **117**, 096404 (2016).
9. B. Bradlyn, *et al.*, *Science* **353** (2016).

10. J. Cano, B. Bradlyn, *Annu. Rev. Condens. Matter Phys.* **12**, 225 (2021).
11. W. Witczak-Krempa, G. Chen, Y. B. Kim, L. Balents, *Annu. Rev. Condens. Matter Phys.* **5**, 57 (2014).
12. S. Paschen, Q. Si, *Nat. Rev. Phys.* **3**, 9 (2021).
13. H.-H. Lai, S. E. Grefe, S. Paschen, Q. Si, *Proceedings of the National Academy of Sciences* **115**, 93 (2018).
14. S. E. Grefe, H.-H. Lai, S. Paschen, Q. Si, *Phys. Rev. B* **101**, 075138 (2020).
15. S. Dzsaber, *et al.*, *Phys. Rev. Lett.* **118**, 246601 (2017).
16. S. Dzsaber, *et al.*, *Proceedings of the National Academy of Sciences* **118** (2021).
17. H. L. Stormer, D. C. Tsui, A. C. Gossard, *Rev. Mod. Phys.* **71**, S298 (1999).
18. L. Chen, *et al.*, *arXiv preprint arXiv:2107.10837* (2021).
19. P. Chandra, P. Coleman, R. Flint, *Nature* **493**, 621 (2013).
20. S. Kirchner, *Advanced Quantum Technologies* **3**, 1900128 (2020).
21. P. Nozieres, A. Blandin, *Journal de Physique* **41**, 193 (1980).
22. D. L. Cox, A. Zawadowski, *Advances in Physics* **47**, 599 (1998).
23. I. Affleck, A. W. W. Ludwig, *Phys. Rev. B* **48**, 7297 (1993).
24. S.-S. Yeh, *et al.*, *Nature Communications* **11**, 4749 (2020).
25. V. J. Emery, S. Kivelson, *Phys. Rev. B* **46**, 10812 (1992).
26. J. M. Maldacena, A. W. Ludwig, *Nuclear Physics B* **506**, 565 (1997).

27. G. Kotliar, D. Vollhardt, *Physics today* **57**, 53 (2004).
28. M. Jarrell, H. Pang, D. L. Cox, K. H. Luk, *Phys. Rev. Lett.* **77**, 1612 (1996).
29. A. Vashist, R. K. Gopal, D. Srivastava, M. Karppinen, Y. Singh, *Phys. Rev. B* **99**, 245131 (2019).
30. X. He, *et al.*, *Phys. Rev. B* **101**, 075106 (2020).
31. H. Hidaka, *et al.*, *Phys. Rev. B* **71**, 073102 (2005).
32. S. H. Curnoe, H. Harima, K. Takegahara, K. Ueda, *Phys. Rev. B* **70**, 245112 (2004).
33. C. Quitmann, *et al.*, *Phys. Rev. B* **38**, 6432 (1988).
34. M. Tsujimoto, Y. Matsumoto, T. Tomita, A. Sakai, S. Nakatsuji, *Phys. Rev. Lett.* **113**, 267001 (2014).
35. A. Sakai, S. Nakatsuji, *J. Phys. Soc. Japan* **80**, 063701 (2011).
36. A. Georges, G. Kotliar, Q. Si, *International Journal of Modern Physics B* **06**, 705 (1992).
37. D. L. Cox, A. E. Ruckenstein, *Phys. Rev. Lett.* **71**, 1613 (1993).
38. J. Kroha, P. Wölfle, *Advances in Solid State Physics* 39 (Springer Berlin Heidelberg, Berlin, Heidelberg, 1999), pp. 271–280.
39. M. H. Hettler, J. Kroha, S. Hershfield, *Phys. Rev. B* **58**, 5649 (1998).
40. F. B. Anders, *Phys. Rev. B* **71**, 121101 (2005).
41. A. A. Abrikosov, L. P. Gorkov, I. E. Dzyaloshinski, *Methods of quantum field theory in statistical physics* (Courier Corporation, 2012).

- 42. V. Gurarie, *Phys. Rev. B* **83**, 085426 (2011).
- 43. Z. Wang, X.-L. Qi, S.-C. Zhang, *Phys. Rev. B* **85**, 165126 (2012).
- 44. Y. Michishita, R. Peters, *Phys. Rev. B* **103**, 195133 (2021).
- 45. Z. Z. Du, C. M. Wang, H.-P. Sun, H.-Z. Lu, X. C. Xie, *Nature Communications* **12**, 5038 (2021).
- 46. H. Sugawara, *et al.*, *Phys. Rev. B* **66**, 134411 (2002).

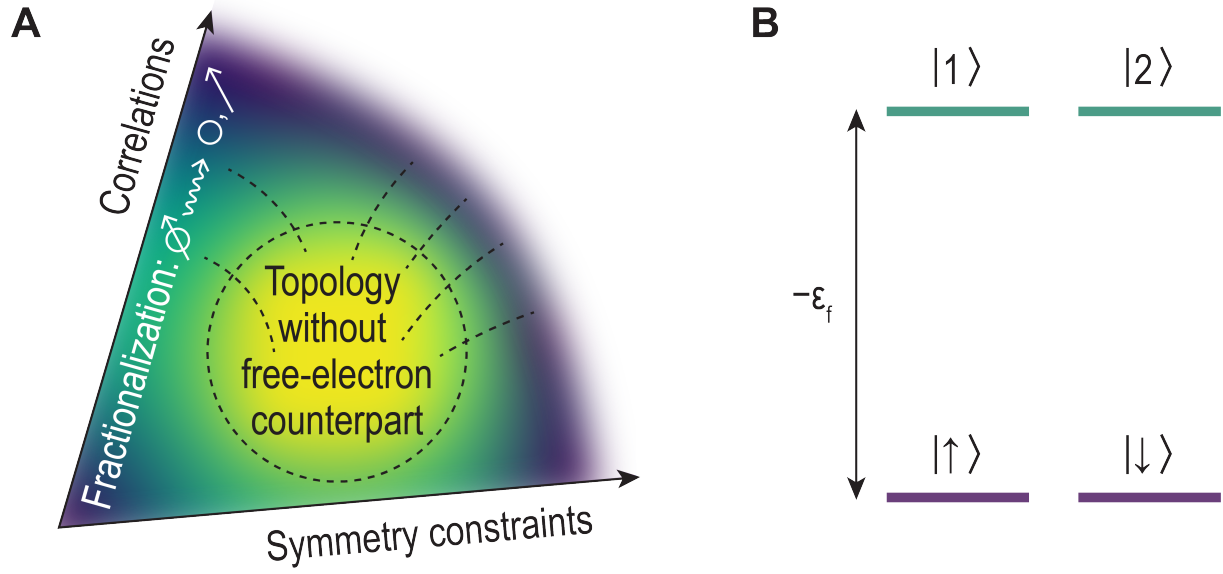


Figure 1: **Illustration of the proposed route for topological phases without free-electron counterpart.** (A) Topological phase without free-electron counterpart that is driven by the cooperation of electron correlations with symmetry constraints. (B) Strongly correlated local degrees of freedom involved in the two-channel Anderson lattice model.

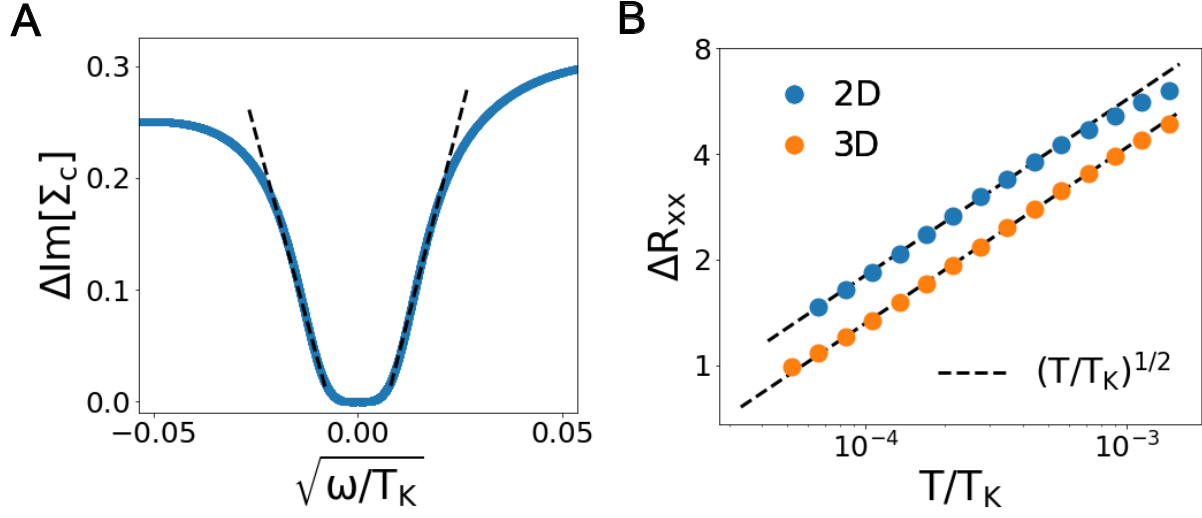


Figure 2: **Breakdown of Landau quasiparticles.** (A) The self-energy (Σ_c) shows a $\sqrt{\omega}$ -dependence at $T/T_K = 4 \times 10^{-5}$ in the 2D kagome lattice. To isolate the frequency dependence, the zero frequency contribution has been subtracted in the plot: $\Delta\text{Im}[\Sigma_c](\omega) = \text{Im}[\Sigma_c](\omega) - \text{Im}[\Sigma_c](0)$. (B) Temperature dependence of the electrical resistivity along the x direction in the 2D and 3D kagome lattices. Both the $\sqrt{\omega}$ and \sqrt{T} dependences characterize the breakdown of Landau quasiparticles.

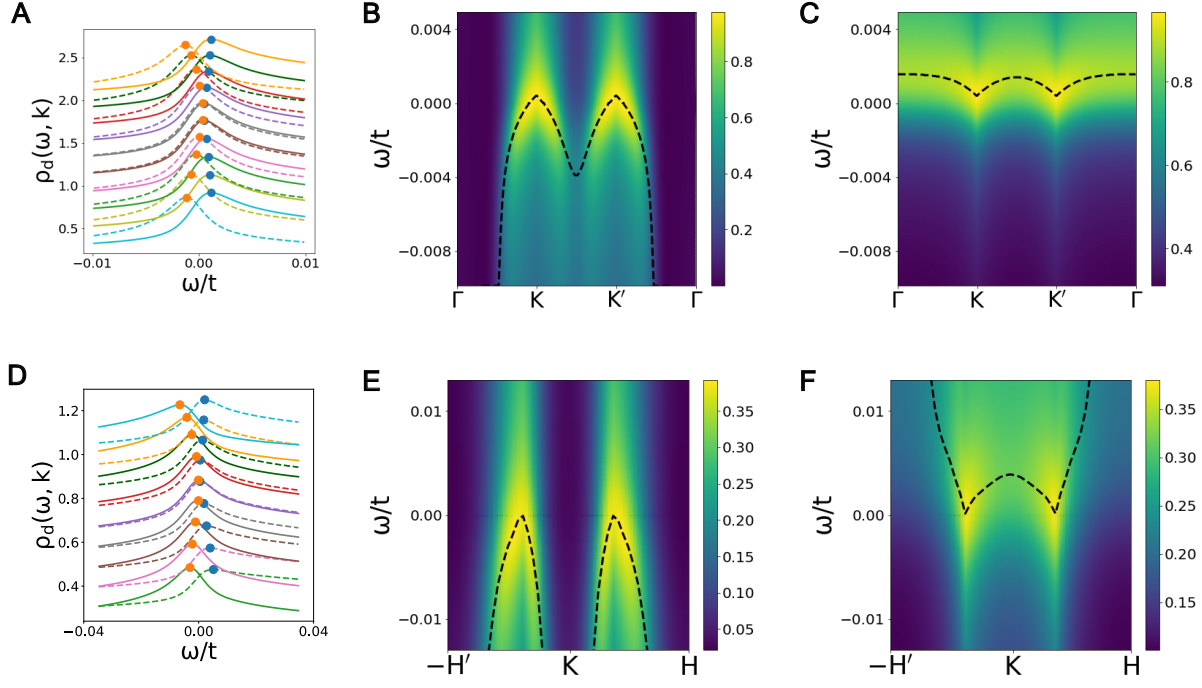


Figure 3: **Emergence of non-Fermi liquid Dirac and Weyl nodes.** (A) The d electron spectral functions (ρ_d) at various \mathbf{k} points near K in the 2D kagome lattice. Solid and dashed lines denote two dispersive modes from two eigenvalues of Green's function. The blue and orange dots label the positions of the spectral peaks, which meet at a Dirac point. Each ρ_d curve has been shifted vertically to avoid overlapping. (B),(C) illustrate the spectral functions of the two Dirac-point-bearing branches. Here, the dashed line denotes the energy spectral peaks. (D),(E),(F) The counterpart results for the Weyl nodes in the 3D kagome lattice. The calculations are done at the temperature $T/T_K = 10^{-3}$ in all cases.

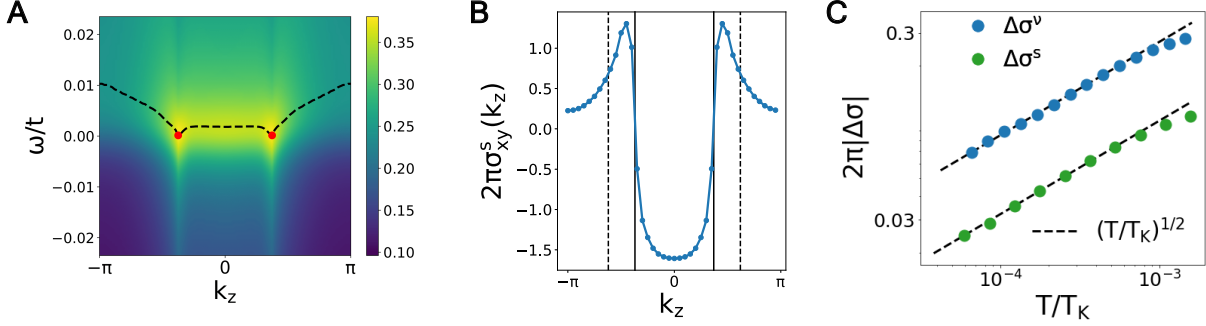


Figure 4: **Characterizing the topological nature of the correlated phases.** (A) The spectrum of the edge mode at $k_x = 4\pi/3$ in the 3D kagome lattice; the two red dots mark the Weyl nodes. (B) In-plane spin-Hall conductivity σ^s_{xy} as a function of k_z in the 3D kagome model. The vertical solid/dashed lines mark the k_z coordinates of the planes in which the Weyl/Dirac nodes reside. A rapid change occurs when k_z crosses the Weyl/Dirac-node-hosting planes. (C) The valley Hall conductivity of the 2D kagome model and the spin Hall conductivity of the 3D kagome model showing a \sqrt{T} dependence. Here, the extrapolated zero-temperature values are subtracted in order to reveal the nature of the T -dependent component.

Supplementary Materials

Gapless electronic topology without free-electron counterpart

Haoyu Hu, Lei Chen, Chandan Setty, Sarah E. Grefe, Andrey Prokofiev,

Stefan Kirchner, Silke Paschen, Jennifer Cano, and Qimiao Si

Materials and Methods

Fig S1 – S8

References (36 – 46, see above)

Materials and Methods

A. Noninteracting band structure

The noninteracting Hamiltonian of the 3D kagome lattice is

$$\begin{aligned}
 H_0 &= \sum \begin{bmatrix} c_{\uparrow}^{\dagger} & c_{\downarrow}^{\dagger} \end{bmatrix} \begin{bmatrix} h(k) - \mu \mathbb{I} & \\ & h^*(-k) - \mu \mathbb{I} \end{bmatrix} \begin{bmatrix} c_{\uparrow} \\ c_{\downarrow} \end{bmatrix} \\
 c_{\sigma} &= \begin{bmatrix} c_{A,\sigma} & c_{B,\sigma} & c_{C,\sigma} \end{bmatrix}^T.
 \end{aligned} \tag{2}$$

Here, A, B, C denote three sublattices marked by $(\frac{1}{4}, \frac{\sqrt{3}}{4}, 0)a, (\frac{1}{2}, 0, 0)a, (\frac{1}{4}, -\frac{\sqrt{3}}{4}, 0)a$ respectively. The hopping matrix in the spin up sector is:

$$\begin{aligned}
 h(k) &= [t - t_{z,2} \cos(k_z)] \\
 &\quad \begin{bmatrix} 0 & [(1+\alpha) + (1-\alpha)e^{-ik_2}] & [(1+\alpha)e^{ik_1} + (1-\alpha)e^{-ik_2}] \\ [(1+\alpha) + (1-\alpha)e^{ik_2}] & 0 & [(1+\alpha)e^{ik_1} + (1-\alpha)] \\ [(1+\alpha)e^{-ik_1} + (1-\alpha)e^{ik_2}] & [(1+\alpha)e^{-ik_1} + (1-\alpha)] & 0 \end{bmatrix} \\
 &\quad - t_z \cos(k_z) \begin{bmatrix} 1 & 0 & 0 \\ 0 & 1 & 0 \\ 0 & 0 & 1 \end{bmatrix} - t_2 \begin{bmatrix} 0 & [e^{i(-k_1-k_2)} + e^{ik_1}] & (1 + e^{i(k_1-k_2)}) \\ [e^{i(k_1+k_2)} + e^{-ik_1}] & 0 & [e^{i(k_1+k_2)} + e^{-ik_2}] \\ [1 + e^{-i(k_1-k_2)}] & [e^{-i(k_1+k_2)} + e^{ik_2}] & 0 \end{bmatrix} \\
 &\quad + [i\lambda + i\lambda_z \cos(k_z)] \begin{bmatrix} 0 & [1 + e^{-ik_2}] & [-e^{ik_1} - e^{-ik_2}] \\ -[1 + e^{ik_2}] & 0 & [1 + e^{ik_1}] \\ [e^{-ik_1} + e^{ik_2}] & -[1 + e^{-ik_1}] & 0 \end{bmatrix},
 \end{aligned}$$

where

$$k_{1/2} = 2\pi(k_x \pm \frac{k_y}{\sqrt{3}}).$$

In addition, t, t_2 are the nearest-neighbor and next-nearest-neighbor intra-layer hopping parameters, t_z and $t_{z,2}$ are the nearest-neighbor and next-nearest-neighbor inter-layer hopping elements. α denotes the anisotropy of t_1 and $t_{z,2}$ hopping that breaks mirror symmetry M_y and inversion symmetry. λ and λ_z are the intra-layer and inter-layer spin orbit couplings, respectively. The corresponding 2D kagome model without spin-orbit coupling and inversion symmetry breaking can be realized by setting $t_z = t_{z,2} = \lambda = \lambda_z = 0, \alpha = 0$ and drop all the terms that contain k_z .

In practice, we set $t_1 = 1, t_2 = 0.3, \mu = -1.0$ for the 2D kagome model. The noninteracting dispersion and Dirac node are shown in Fig. S1B. At the high symmetry point K/K' , three bands form $\Gamma_1 \oplus \Gamma_3$ representations of the little group C_{3v} , where Γ_3 is a two-dimensional irreducible representation and thus protects the Dirac node.

For the 3D model, we set $t_1 = 0.29, t_2 = 0.14, t_z = -0.17, t_{z,2} = 0.26, \lambda = 0.43, \lambda_z = 0.06, \alpha = 1.4, \mu = -1.09$. As shown in Fig. S1C and Fig. S1D, we observe two Weyl nodes at $(1/3, 1/3, z), (2/3, 2/3, -z)$, two anti-Weyl nodes at $(1/3, 1/3, -z), (2/3, 2/3, z)$, and two Dirac nodes at $(0, 0, \pm z')$ where $z \approx 0.19, z' \approx 0.32$. Weyl and Dirac nodes are all protected by C_{3z} symmetry. In Fig. S1E and Fig. S1F, we label the relevant bands by their eigenvalues of C_{3z} symmetry, where $\eta = e^{i2\pi/3}$. The C_{3z} symmetry excludes the hybridization between the two bands with different eigenvalues, and thus protects the nodes. The bands also hold Dirac nodes that are two-fold degenerate, along a high symmetry line $(-A-\Gamma-A)$, due to the mirror symmetry M_z and time-reversal symmetry. The eigenvalues inside (outside) the brackets are for the spin-up (spin-down) sector.

B. Dynamical mean-field theory and dynamical large- N saddle-point equations

In order to solve the lattice mode, we first introduce the auxiliary-particle representation of the projected local electron annihilation operator: $Pd_{i,\sigma,\alpha}P = f_{i,\sigma}b_{i,\alpha}^\dagger$. Here, $f_{i,\sigma}$ is a pseudo-fermion annihilation operator and $b_{i,\alpha}^\dagger$ is a pseudo-boson creation operator. The Hilbert space of the d electron can be expressed as: $|\sigma\rangle = f_\sigma^\dagger|\text{vac}\rangle$, $|\alpha\rangle = b_\alpha^\dagger|\text{vac}\rangle$ with the vacuum state $|\text{vac}\rangle$. There is also a local constraint $Q_i = \sum_\sigma f_{i,\sigma}^\dagger f_{i,\sigma} + \sum_\alpha b_{i,\alpha}^\dagger b_{i,\alpha} = 1$.

The Anderson lattice Hamiltonian is mapped to a self-consistent impurity model (36):

$$\begin{aligned}
S_{imp} = & \int \sum_{\sigma,\alpha} c_{\sigma,\alpha}^\dagger(\tau) G_0(\tau, \tau')^{-1} c_{\sigma,\alpha}(\tau') d\tau d\tau' \\
& + \int \left[\sum_\sigma f_\sigma^\dagger(\tau) (\partial_\tau - \epsilon_f) f_\sigma(\tau) + \sum_\alpha b_\alpha^\dagger(\tau) \partial_\tau b_\alpha(\tau) \right] d\tau \\
& + \int V \sum_{\sigma,\alpha} (c_{\alpha,\sigma}^\dagger(\tau) f_\sigma(\tau) b_\alpha^\dagger(\tau) + h.c.) d\tau \\
& + \int i\lambda(\tau) \left(\sum_\sigma f_\sigma^\dagger(\tau) f_\sigma(\tau) + \sum_\alpha b_\alpha^\dagger(\tau) b_\alpha(\tau) - Q \right) d\tau. \tag{3}
\end{aligned}$$

Here, λ is a Lagrangian multiplier enforcing the pseudoparticle constraint. Whereas G_0 is the bath function of the conduction electrons, which is determined from the DMFT equations:

$$\begin{aligned}
G_{c,loc}(\omega) &= \frac{1}{N} \sum_{\mathbf{k}} \frac{1}{\omega - t_{\mathbf{k}} - \Sigma_c(\omega)} \\
G_0^{-1}(\omega) - G_{c,loc}^{-1}(\omega) &= \Sigma_c(\omega), \tag{4}
\end{aligned}$$

where $t_{\mathbf{k}}$ is the Fourier transformation of the hopping matrix, $G_{c,loc}(\omega)$ is the local Green's function of the c electrons, $\Sigma_c(\omega)$ is the associated self-energy which is taken to be local, i.e., \mathbf{k} -independent within the DMFT.

The impurity model is solved via the saddle point equations (37–40) of a dynamical large- N limit (with a generalization to an $\text{SU}(N)$ symmetry for the local moments and an $\text{SU}(N) \times \text{SU}(M)$

symmetry for the conduction electrons and taking the large- N , M limit with $N/M = 1$). Here, the self-energies of the pseudo-fermion and pseudo-boson are

$$\begin{aligned}\Sigma_f(\omega) &= MV^2 \int \rho_0(\omega - \epsilon) f(\epsilon - \omega) G_b(\epsilon) d\epsilon \\ \Sigma_b(\omega) &= NV^2 \int \rho_0(\epsilon - \omega) f(\epsilon - \omega) G_f(\epsilon) d\epsilon\end{aligned}$$

where ρ_0 is the density of states of the bath function G_0 and $f(x)$ is the Fermi-Dirac function. In conjunction with the Dyson equations for the pseudo-particle propagators G_f, G_b ,

$$\begin{aligned}G_f^{-1}(\omega) &= \omega - \epsilon_f - \lambda - \Sigma_f(\omega) \\ G_b^{-1}(\omega) &= \omega - \lambda - \Sigma_b(\omega)\end{aligned}$$

we have a complete set of equations. These equations are known to capture the correct asymptotic low-energy behavior –including the correct non-Fermi liquid exponents – of the multi-channel Kondo/Anderson models (37).

In practice, we take $V = 1.0$, $\epsilon_f = -0.5$ for the 2D kagome model and $V = 1.5$, $\epsilon_f = -1.0$ for the 3D kagome model. We solve the DMFT self-consistent equation by varying the bath function $G_{c,0}$ and stop the procedure when the difference between two iterations is less than 1%.

C. Non-Fermi liquid properties

In Fig. S2A-Fig. S2D, we show the local spectral functions of the pseudo-bosons and pseudo-fermions of both the 2D and 3D kagome lattices. We observe an ω/T scaling with

$$\begin{aligned}\rho_f(\omega, T) &= \left(\frac{T}{T_K}\right)^{1/2} g_f(\omega/T) \\ \rho_b(\omega, T) &= \left(\frac{T}{T_K}\right)^{1/2} g_b(\omega/T)\end{aligned}\tag{5}$$

where $g_f(x), g_b(x)$ are universal functions. In addition, to illustrate the power-law dependence, Fig. S3A and Fig. S3B depict ρ_b vs. frequency at a low temperature.

The self-energy Σ_c encodes the non-Fermi liquid behavior. Due to the symmetry requirement, the local self-energy Σ_c is diagonal in spin, sublattice and channel spaces, which simplifies the analysis. As shown in Fig. S4A, Fig. S4B and Fig. S4C, $\text{Im}[\Sigma_c](\omega)$ has a peak near the Fermi energy. We find that this peak is approximately represented by a Lorentzian function: $\text{Im}[\Sigma_c](\omega) \sim \frac{A\gamma^2}{\omega^2 + \gamma^2}$, where A and γ are the amplitude and width of peak respectively. Combining this approximation with Kramers-Kronig relation, we obtain $\Sigma_c(\omega) \sim \frac{A\gamma}{\omega - i\gamma}$. In addition, there is a sub-leading $\sqrt{|\omega|}$ behavior in the low energy limit as shown in Fig. S4D, Fig. S4B and Fig. S4F. Including this contribution, we have the following ansatz of the self-energy

$$\Sigma_c(\omega) \sim \frac{A\gamma}{\omega - i\gamma} + c\sqrt{|\omega|} \theta(|\omega| < \Lambda) \quad (6)$$

where $\theta(x)$ is the step function. Λ is the energy cutoff below which the $\sqrt{|\omega|}$ behavior appears. The non-Fermi liquid behavior of the self-energy still leads to a band reconstruction in the interacting model, as shown in Fig. S5.

Combining the self-energy ansatz and symmetry group, we are able to analyze the structure of the Green's function near the Dirac and Weyl nodes. For both cases, near the crossing momentum \tilde{k} , we have

$$\tilde{P}G_c^{-1}(\omega, \tilde{k}+k)\tilde{P} \approx U^\dagger \begin{bmatrix} \omega - E_0 - v_z k_z - \frac{A\gamma}{\omega - i\gamma} - c\sqrt{|\omega|} & -v_x k_x + i v_y k_y \\ -v_x k_x - i v_y k_y & \omega - E_0 + v_z k_z - \frac{A\gamma}{\omega - i\gamma} - c\sqrt{|\omega|} \end{bmatrix} U$$

where \tilde{P} is the projection matrix that only keeps the relevant bands, U is a unitary matrix that brings the dispersion near a Weyl/Dirac node into the canonical form and E_0 is the energy of the noninteracting Weyl/Dirac nodes. For the Dirac nodes in 2D, we set $v_z = 0$ and ignore the two-fold degeneracy in spin space. The corresponding spectral functions would have peaks near Fermi energy at $\omega \sim \gamma A/E_0(1 \pm \sqrt{v_x^2 k_x^2 + v_y^2 k_y^2 + v_z^2 k_z^2}/E_0)$. Each peak corresponds to one branch of the Dirac/Weyl node in the heavy bands.

D. Symmetry of Green's function

The general properties of the single-particle Green's function (41, 42) allow for the introduction of Green's function eigenvectors and eigenfunctions in multi-band cases (43). Consider the Green's functions:

$$\begin{aligned}[G_c(\omega, \mathbf{k})]_{ij} &= -\langle c_{i,\mathbf{k},\omega} c_{i,\mathbf{k},\omega}^\dagger \rangle \\ [G_d(\omega, \mathbf{k})]_{ij} &= -\langle d_{i,\mathbf{k},\omega} d_{i,\mathbf{k},\omega}^\dagger \rangle,\end{aligned}$$

where i denotes sublattice and spin index. Due to the $SU(2)$ channel symmetry, we omit the channel index here. In the spin-1/2 kagome system with three sublattices per unit cell, $G_{c/d}(\omega, \mathbf{k})$ would be a 6×6 matrix. From $U(1)$ spin symmetry, $G_{c/d}$ is block diagonalized into up and down sectors $G_{c/d} = \text{diag}[G_{c/d,\uparrow}, G_{c/d,\downarrow}]$. In the 2D kagome model without any spin-orbit coupling, there is an additional $SU(2)$ spin symmetry that requires $G_{c/d,\uparrow} = G_{c/d,\downarrow}$ so that the spin index can be dropped as well in this case.

We define the i -th dispersive mode as the i -th eigenvalue $g_{c/d,i}(\omega, \mathbf{k})$ and i -th eigenvector $v_{c/d,i}(\omega, \mathbf{k})$ of $G_{c/d}(\omega, \mathbf{k})$ ($G_{c/d} v_{c/d,i} = g_{c/d,i} v_{c/d,i}$). The corresponding spectral function of the i -th mode is $\rho_{c/d,i}(\omega, \mathbf{k}) = \frac{1}{\pi} \text{Im}[g_{c/d,i}(\omega - i0^+, \mathbf{k})]$. It's also worth mentioning that, in the non-interacting limit, $\{v_{c,i}(\omega, \mathbf{k})\}_i$ coincide with the eigenvectors of the hopping matrix and $\rho_{c,i}(\omega, \mathbf{k}) = \delta(\omega - \epsilon_{\mathbf{k},i})$ where $\epsilon_{\mathbf{k},i}$ are the eigenvalues of the hopping matrix.

Under the space group symmetry $g : c_{\mathbf{k}} \rightarrow U_g^\dagger c_{g\mathbf{k}}, d_{\mathbf{k}} \rightarrow U_g^\dagger d_{g\mathbf{k}}$, the Green's function satisfies

$$\begin{aligned}G_c(\omega, \mathbf{k}) &= U_g^\dagger G_c(\omega, g\mathbf{k}) U_g \\ G_d(\omega, \mathbf{k}) &= U_g^\dagger G_d(\omega, g\mathbf{k}) U_g\end{aligned}$$

Thus, similarly to the Bloch functions of the noninteracting case, $\{v_{c/d,i}(\omega, \mathbf{k})\}_i$ form a representation of the space group. We can derive the symmetry properties from them in a similar

manner.

Based on the eigenvectors and eigenvalues, we now prove that the Dirac nodes in the 2D kagome model and the Weyl (Dirac) nodes in the 3D kagome model are both protected by crystalline symmetry, but via different mechanisms. Since single-particle excitations are composite fermions, it is enough to focus on G_d .

In the 2D kagome lattice, the Dirac nodes are symmetry enforced. $\{v_{d,i}(\omega, \mathbf{k} = K/K')\}_i$ forms the $\Gamma_1 \oplus \Gamma_3$ representation of the little group $G_{K/K'} = C_{3v}$. Due to the $SU(2)$ symmetry, we can ignore the spin index and use a spinless representation here. The two-dimensional irreducible representation Γ_3 enforces a two-fold-degenerate spectrum at the K/K' point. Consequently, two dispersive modes have to coincide with each other at the K/K' point as shown in Fig. 3A.

The Weyl nodes in 3D kagome model comes from the band inversion mechanism. Along the high symmetry line $K-H$, we can assign an eigenvalue of C_{3z} to each dispersive mode. In Fig. 3D, two modes with left-moving and right-moving peaks have symmetry eigenvalues η^3 and η^5 , respectively, where $\eta = e^{i2\pi/3}$. The different eigenvalues would protect the crossing of the two modes under symmetry-preserved perturbations. The similar mechanism protects the Weyl nodes on $-H-K'-H'$ and Dirac nodes on $-A-\Gamma-A$.

E. Edge modes

To evaluate the edge mode in the 3D kagome model, we take a slab geometry with 50 unit cells and open boundary along y direction. In the noninteracting limit, this leads to an edge mode above the Fermi energy.

In the interacting model, we consider the Green's function $[G_d(\omega, k_x, k_z)]_{y_1\alpha_1, y_2\alpha_2}$ that is a 300×300 matrix, where y_i is the coordination of unit-cell along the y direction and α_i is the sublattice and spin index. Through diagonalizing the Green's function matrix, we find

the eigenvalues $\{g_i(\omega, k_x, k_z)\}_i$ and eigenvectors $\{[v_i(\omega, k_x, k_z)]_{y\alpha}\}_i$. For a local self-energy, $[v_i(\omega, k_x, k_z)]_{y\alpha}$ becomes ω independent and describes the real-space distribution of the corresponding mode. Numerically, we identify an edge mode that decays exponentially in the real space as shown in Fig. S6A. The corresponding spectral function $\text{Im}[g_i(\omega, k_x, k_z)]/\pi$ is shown in Fig. 4A.

F. Hall conductivity

Within the DMFT approach, in which vertex corrections are formally suppressed, the valley Hall conductivity σ^ν is

$$\sigma^\nu = \frac{1}{4\pi^2} \int_{|\mathbf{k}-K|<C} \sum_{m,n} \tilde{\Omega}_{mn}(\mathbf{k}) - \frac{1}{4\pi^2} \int_{|\mathbf{k}-K'|<C} \sum_{m,n} \tilde{\Omega}_{mn}(\mathbf{k}), \quad (7)$$

where the \mathbf{k} integration is taken in a finite region near K/K' with cutoff $C = \pi/2$. n, m are band indices. From top to bottom, we label the bands by 1, 2, 3 in the 2D kagome model. In addition,

$$\begin{aligned} \tilde{\Omega}_{mn}(\mathbf{k}) &= i \lim_{\nu \rightarrow 0} \frac{d}{d(i\nu)} \sum_{i\omega} \frac{(V_{\mathbf{k}}^\dagger \partial_{k^x} t_{\mathbf{k}} V_{\mathbf{k}})_{nm} (V_{\mathbf{k}}^\dagger \partial_{k^y} t_{\mathbf{k}} V_{\mathbf{k}})_{mn}}{[i\omega + i\nu - \epsilon_{\mathbf{k},n} - \Sigma_c(i\omega)][i\omega - \epsilon_{\mathbf{k},m} - \Sigma_c(i\omega)]} \\ &= i \lim_{\nu \rightarrow 0} \frac{d}{d(i\nu)} \sum_{m,n} \frac{[A_{\mathbf{k},mn}^x A_{\mathbf{k},nm}^y - A_{\mathbf{k},nm}^x A_{\mathbf{k},mn}^y] (\epsilon_{\mathbf{k},n} - \epsilon_{\mathbf{k},m})^2}{[i\omega + i\nu - \epsilon_{\mathbf{k},n} - \Sigma_c(i\omega)][i\omega - \epsilon_{\mathbf{k},m} - \Sigma_c(i\omega)]}. \end{aligned} \quad (8)$$

$V_{\mathbf{k}}, \{\epsilon_{\mathbf{k},n}\}_n$ are the eigenvectors and eigenvalues of hopping matrix $t_{\mathbf{k}}$. $A_{mn,\mathbf{k}}^\mu = i\langle u_{m,\mathbf{k}} | \partial_{k^\mu} | u_{n,\mathbf{k}} \rangle$ is a Berry connection.

In the noninteracting limit, the lowest band that is below the Fermi energy contributes a positive σ^ν . The top two bands are above the Fermi energy near $K(K')$ and, thus $\tilde{\Omega}_{12}$ and $\tilde{\Omega}_{21}$ are zero. Once we turn on the hybridization V , dispersive modes develop near the Fermi energy and generate nonzero $\tilde{\Omega}_{12}$ and $\tilde{\Omega}_{21}$. We can extract the contributions from $\tilde{\Omega}_{12}$ and $\tilde{\Omega}_{21}$ and define σ_{12}^ν

$$\sigma_{12}^\nu = \frac{1}{4\pi^2} \int_{|\mathbf{k}-K|<\Lambda} (\tilde{\Omega}_{12}(\mathbf{k}) + \tilde{\Omega}_{21}(\mathbf{k})) - \frac{1}{4\pi^2} \int_{|\mathbf{k}-K'|<\Lambda} (\tilde{\Omega}_{12}(\mathbf{k}) + \tilde{\Omega}_{21}(\mathbf{k})).$$

σ_{12}^ν is part of σ^ν that is directly generated by the interactions. The evolution of σ^ν and σ_{12}^ν as a function of hybridization is shown in Fig. S6B.

For the spin Hall conductivity, we consider the in-plane contribution of each k_z : $\sigma_{xy}^s(k_z)$

$$\sigma_{xy}^s(k_z) = \frac{1}{4\pi^2} \int_{k_x, k_y} \sum_{m, n \in \uparrow} \tilde{\Omega}_{mn}(k_x, k_y, k_z) - \frac{1}{4\pi^2} \int_{k_x, k_y} \sum_{m, n \in \downarrow} \tilde{\Omega}_{mn}(k_x, k_y, k_z) \quad (9)$$

where the first (second) terms sum over bands with spin up (down). The full bulk contribution is obtained via $\sigma_{xy}^s = \int_{k_z} \sigma^s(k_z)$.

G. Non-linear Hall effect

We now turn to the non-linear Hall effect in the non-Fermi liquid phase. Using the Green's function approach (44), the non-linear Hall conductivity is

$$\begin{aligned} \chi_{xyy} = & -\frac{1}{2\pi} \int_{\mathbf{k}, \epsilon} \text{Im} \left\{ \text{Tr} \left[\partial_\epsilon f(\epsilon) u_x \partial_\epsilon G_c(\epsilon - i0^+) u_y G_c(\epsilon - i0^+) u_y G_c(\epsilon + i0^+) \right. \right. \\ & + \partial_\epsilon f(\epsilon) u_x \partial_\epsilon G_c(\epsilon - i0^+) u_{yy} G_c(\epsilon + i0^+) + f(\epsilon) u_x \partial_\epsilon^2 G_c(\epsilon - i0^+) u_{yy} \\ & \left. \left. + 2f(\epsilon) u_x \partial_\epsilon [G_c(\epsilon - i0^+) u_y G_c(\epsilon - i0^+)] u_y G_c(\epsilon + i0^+) \right] \right\}, \end{aligned} \quad (10)$$

where $f(\epsilon)$ is the Fermi-Dirac function, and $u_{\mu_1 \mu_2 \dots \mu_n} = \partial_{k_{\mu_1} k_{\mu_2} \dots k_{\mu_n}}^n t_{\mathbf{k}}$. Each term contains a product of three Green's functions with two derivatives of ϵ . In the asymptotic region $c_{IR} < \omega \ll T_K$ where scaling behaviors appear, $G_c(\epsilon) \sim g_0 + g_1 \sqrt{|\epsilon|}$. c_{IR} acts as an infrared cutoff. The integral behaves as $\sim \epsilon^{-3/2} d\epsilon$. (Note that at least one derivative is acting on the Green's function.) Transforming to the temperature behaviors, we would expect $\sim 1/\sqrt{T}$ in the scaling region $c_{IR} < T \ll T_K$. To more explicitly observe this $\sim 1/\sqrt{T}$ behaviors, we consider the Green's function near the Weyl node $\tilde{\mathbf{k}}$

$$G_c(\omega, \mathbf{k} + \tilde{\mathbf{k}})^{-1} \approx [\omega - h_0 - \Sigma_c(\omega)] \mathbb{I} - h_x \sigma^x - h_y \sigma^y - h_z \sigma^z,$$

where $\Sigma_c(\omega)$ is the self-energy. $\sigma^{x,y,z}$ are Pauli matrices in the 2×2 subspace that hold Weyl node. h_0, h_x, h_y, h_z are functions of momentum. At the Weyl node, $h_0(\tilde{\mathbf{k}}) = E_0, h_x(\tilde{\mathbf{k}}) =$

$h_y(\tilde{\mathbf{k}}) = h_z(\tilde{\mathbf{k}}) = 0$. The eigenvalues of the Green's function matrix are

$$g_{\pm}^{-1} = \omega - \epsilon_{\pm} - \Sigma_c(\omega)$$

$$\epsilon_{\pm} = h_0 \pm \sqrt{h_x^2 + h_y^2 + h_z^2},$$

where $\Sigma_c(\omega)$ is the self-energy and has non-Fermi liquid behavior. We also introduce the velocity matrix: $v_{\mu}^{\alpha\gamma} = (V^{\dagger} \partial_{k^{\mu}} t_{\mathbf{k}} V)_{\alpha\gamma}$, where $t_{\mathbf{k}} = h_0 \mathbb{I} + h_x \sigma^x + h_y \sigma^y + h_z \sigma^z$ is the hopping matrix and V is the matrix formed by the eigenvectors of the hopping matrix.

Here, we focus on the intrinsic contributions from the Berry curvature (45). However, all the other contributions produce the same $1/\sqrt{T}$ behavior. The intrinsic contributions reads (from the first term of Eq. 10),

$$\chi_{xyy}^{in} = -\frac{1}{2\pi} \int_{\mathbf{k}} \int d\epsilon \frac{\partial f(\epsilon)}{\partial \epsilon} \text{Im} \left\{ \text{Tr} \left[\begin{aligned} & v_x^{+-} v_y^{-+} v_y^{++} \partial_{\epsilon} g_{-}(\epsilon + i0^{+}) g_{+}(\epsilon + i0^{+}) g_{+}(\epsilon - i0^{+}) \\ & + v_x^{-+} v_y^{++} v_y^{+-} \partial_{\epsilon} g_{+}(\epsilon + i0^{+}) g_{+}(\epsilon + i0^{+}) g_{-}(\epsilon - i0^{+}) \end{aligned} \right] \right\}.$$

Due to the pre-factor $\frac{\partial f(\epsilon)}{\partial \epsilon}$, it is sufficient to focus on the low-energy contribution. Since the self-energy behaves as $\text{Im}[\Sigma_c] \sim a + b\sqrt{|\omega|}$, approximately we have

$$\chi_{xyy}^{in} = -\frac{1}{2\pi} \int_{\mathbf{k}} \int_{\epsilon} \frac{\partial f(\epsilon)}{\partial \epsilon} \Omega_{xy}^{+} v_y^{++} [a_0 + \frac{a_1}{\sqrt{|\epsilon|}} + o(\epsilon)]$$

where $a_1 \approx \pi(\rho_0 \frac{\sqrt{h_x^2 + h_y^2 + h_z^2}}{h_0})^3 \frac{1}{\sqrt{\Lambda}}$ and Λ is the low energy scale of $\sqrt{|\omega|}$ behaviors and ρ_0 is the density of state near zero Fermi energy. After integrating over ϵ , we have

$$\chi_{xyy}^{in} = \frac{1}{\sqrt{T}} \cdot \left[\frac{-1.34}{2\pi} \int_{\mathbf{k}} \Omega_{xy}^{+} v_y^{++} a_1 \right] + \dots \quad (11)$$

where $\Omega_{xy}^{+} = i\langle \partial_x u_{+} | \partial_y u_{+} \rangle - i\langle \partial_y u_{+} | \partial_x u_{+} \rangle$ is the Berry curvature.

H. Candidate materials

We have identified three candidate materials, PrBi (30), PrFe₄P₁₂ (31), and UPt₃Au₂ (33), to realize the correlated topological phases predicted here. They crystallize in the space groups

#225, #204, and #216, respectively, which all allow for a Γ_3 non-Kramers doublet ground state of the Pr^{3+} or U^{4+} $4f^2$ wave function. The former two are centrosymmetric and candidate correlated Dirac semimetals, whereas the latter is noncentrosymmetric and thus a candidate correlated Weyl semimetal.

In PrBi, evidence for a Γ_3 ground state was provided by fitting a crystal electric field (CEF) model to temperature-dependent magnetic susceptibility data; the assignment was supported by a much better agreement of the specific heat data with this than other possible CEF level schemes (30). A low charge carrier concentration was evidenced from quantum oscillation experiments (30). For $\text{PrFe}_4\text{P}_{12}$, key evidence is summarized in Fig. S7. A non-magnetic CEF ground state doublet is suggested by the antiferroquadrupolar ordering at low temperatures (panel A) (31). Strong Kondo coupling was evidenced by a large Sommerfeld coefficient determined from specific heat data (46), and is confirmed by the large A coefficient of the Fermi liquid T^2 form seen in electrical resistivity data under applied pressure and magnetic field (inset of panel B). Finally, under finite pressure, the material shows an upturn of the electrical resistivity with decreasing temperature, *i.e.*, it ceases to be metallic. We thus anticipate that $\text{PrFe}_4\text{P}_{12}$ under finite pressure and PrBi under ambient pressure may fulfill the theoretical requirements for topological two-channel Kondo systems. Finally, UPt_3Au_2 shows a moderately enhanced Sommerfeld coefficient of 60 mJ/mol/K², and an only very weakly temperature-dependent electrical resistivity (33) (see Fig. S8), that may point to the presence of Kondo interaction in a reduced carrier concentration setting.

I. Space group symmetry constraints in the candidate materials

As discussed in the main text, PrBi (29, 30) and $\text{PrFe}_4\text{P}_{12}$ (31, 32) have space groups #225 and #204, respectively. Whereas UPt_3Au_2 (33), which has broken inversion symmetry, has space group #216. These space groups allow for Dirac or Weyl points. For example, in PrBi, if

two bands with crossing point have different eigenvalues under the 2_{010} rotational symmetry, it would be a symmetry protected Dirac node; this symmetry-based argument is manifested in the DFT calculations (albeit without treating correlation effects), in which a band crossing occurs on the Γ - X line (29). Similarly, the 3_{111}^+ rotational symmetry could protect Dirac nodes on the Γ - H line in $\text{PrFe}_4\text{P}_{12}$. Likewise, the 2_{100} rotational symmetry could protect Weyl nodes on the X - W line of UPt_3Au_2 .

Supplementary Figures

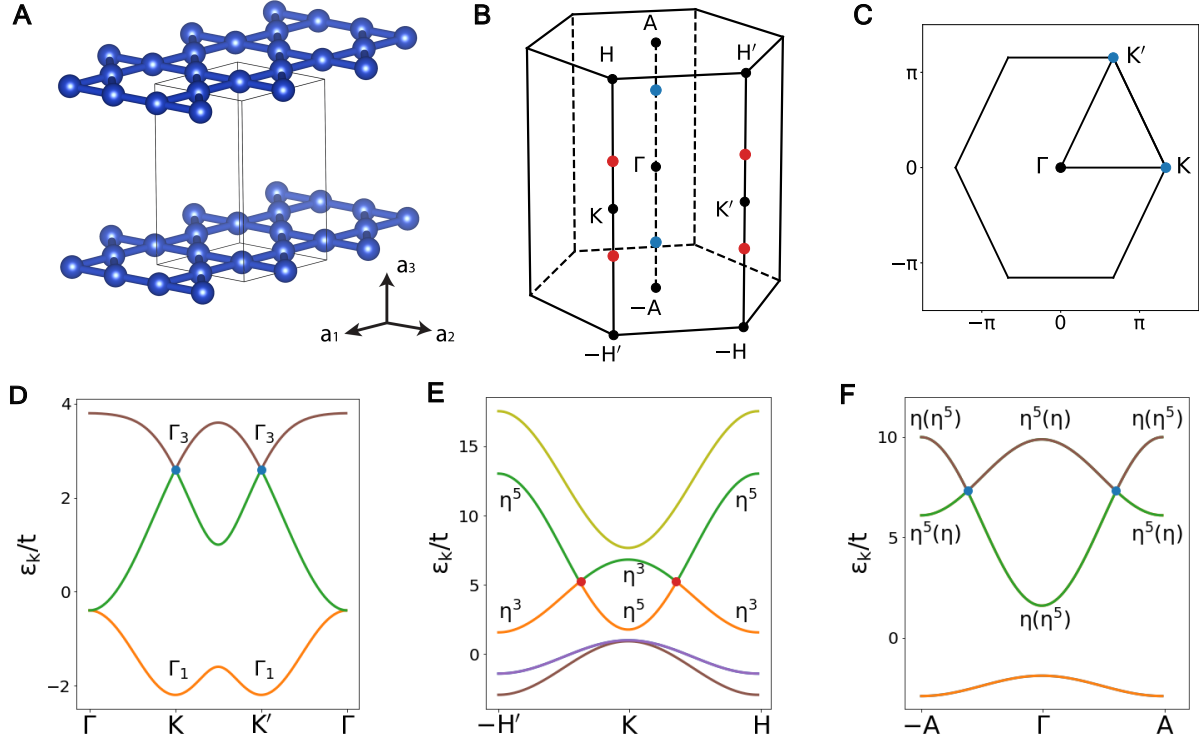


Figure S1: **Lattice structure and the noninteracting dispersion.** (A) The 3D kagome lattice. (B) The first Brillouin zone of the 3D kagome lattice, where red and blue dots denote the Weyl nodes and Dirac nodes, respectively. (C) The first Brillouin zone of the 2D kagome lattice, where the blue dots denote the Dirac nodes. (D) Dispersion of the 2D kagome lattice. (E), (F) Dispersion of the 3D kagome lattice. The relevant bands are marked by their eigenvalues of the C_{3z} symmetry, where $\eta = e^{i2\pi/3}$.

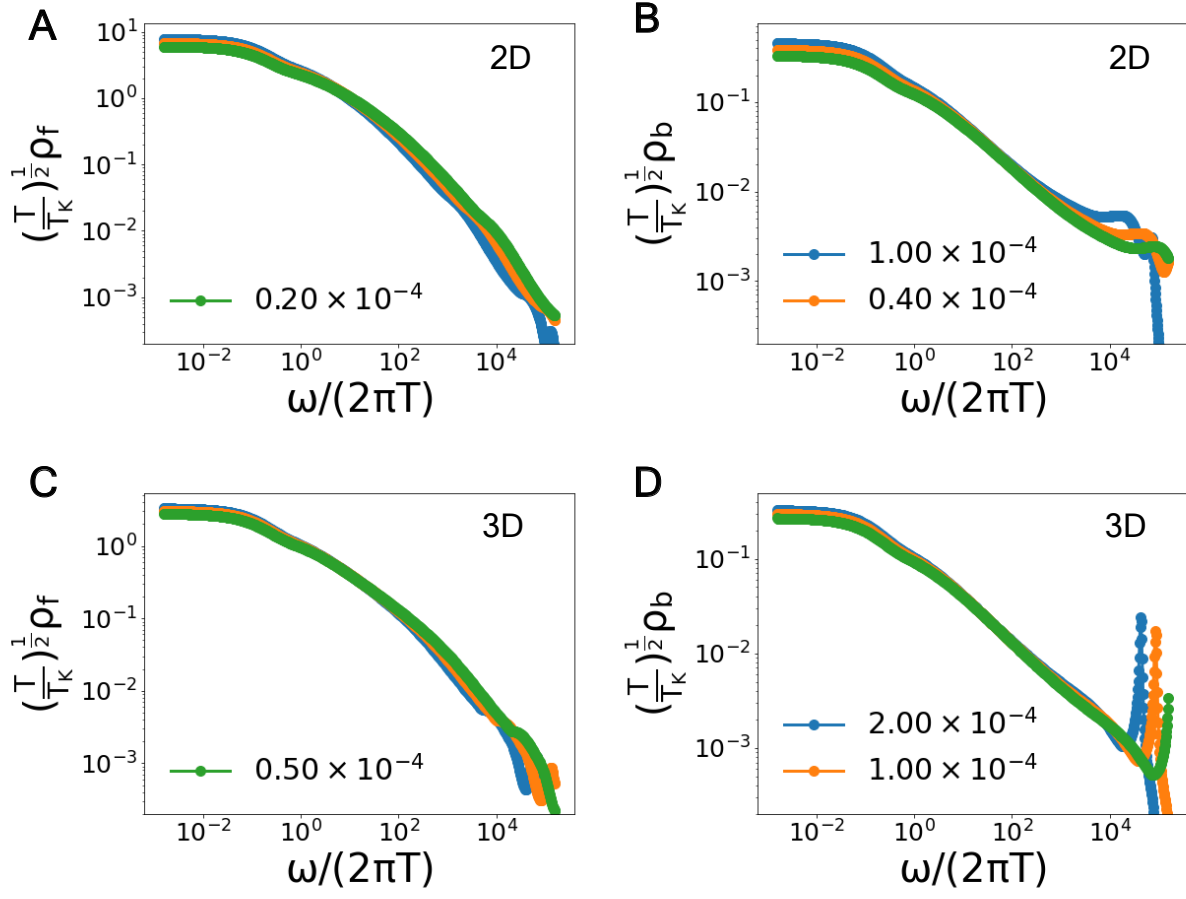


Figure S2: **Dynamical scaling behavior.** (A), (B) spectral functions of ρ_f and ρ_b in the 2D kagome lattice at various temperatures. (C), (D) show the counterpart results for the 3D kagome lattice.

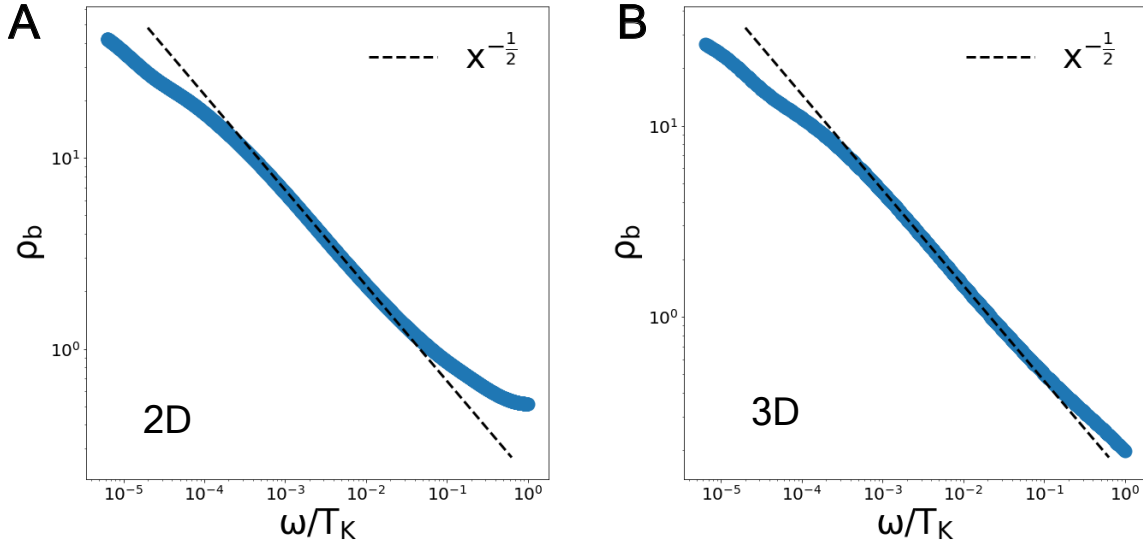


Figure S3: **Power-law behavior of the pseudo-particle spectral function.** The spectral function ρ_b is shown to depend on frequency in a power-law form, $\omega^{-1/2}$, for the 2D (A) and 3D (B) kagome lattices. The power-law form operates for about two decades of frequency. The deviation at high frequencies captures the effect of the ultraviolet energy cutoff. That at low frequencies reflects a nonzero (albeit very low) temperature where the calculation is performed ($T = 10^{-5} T_K$).

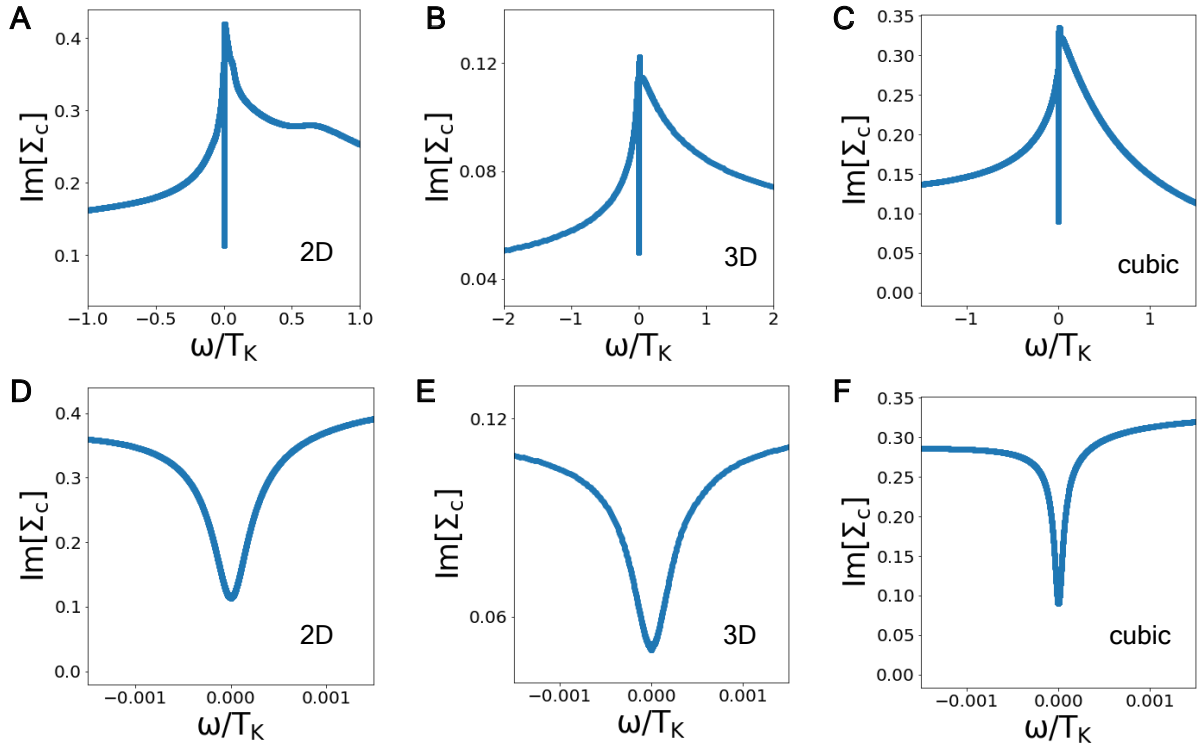


Figure S4: **Non-Fermi liquid behavior of the self-energy.** The imaginary part of the self-energy in the 2D kagome lattice (A), (D), 3D kagome lattice (B), (E) and cubic lattice (C), (F).

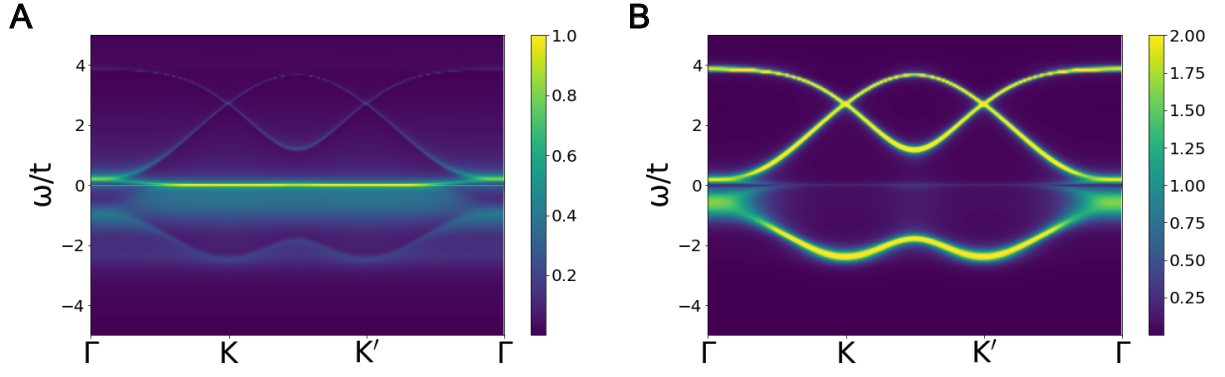


Figure S5: **Spectral functions in the interacting model.** (A) and (B) show the spectral functions of the d and c electrons in the 2D kagome lattice at $T/T_K = 10^{-3}$. We can observe band reconstruction near the Fermi energy.

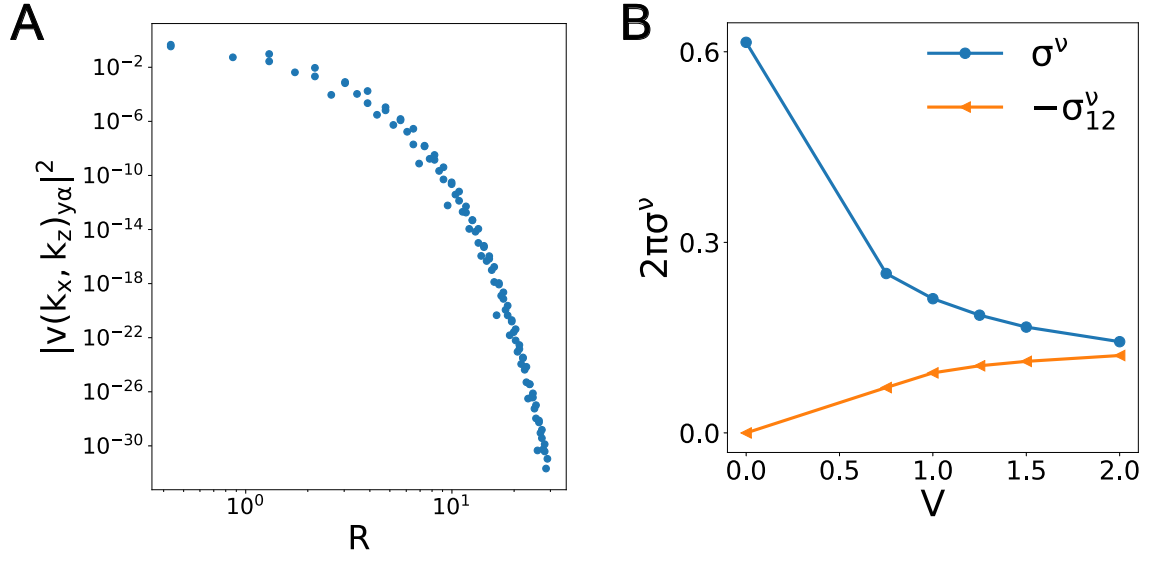


Figure S6: **Topological property.** (A) Exponentially decay of the edge-mode eigenvector $v(k_x = 4\pi/3, k_z = 0)_{\alpha y}$. R denotes the distance to the edge. (B) Valley Hall conductivity as a function of V in the 2D kagome model with fixed $V/\epsilon_f = -0.5$ at $T/T_K = 10^{-3}$.

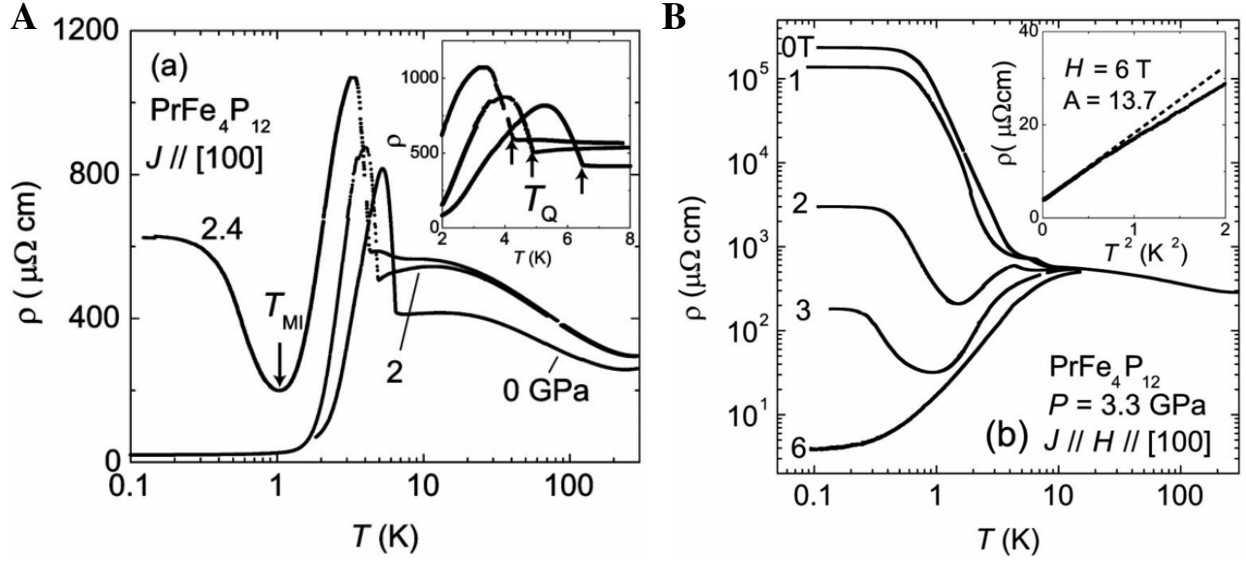


Figure S7: **Candidate two-channel Kondo material $\text{PrFe}_4\text{P}_{12}$.** (A) Temperature-dependent electrical resistivity at ambient pressure and at 2 GPa and 2.4 GPa, revealing that the transition temperature T_Q of the phase with antiferroquadrupolar order is successively suppressed with increasing pressure (see inset). At lower temperatures, a resistivity upturn is observed below T_{MI} . (B) Temperature-dependent electrical resistivity at 3.3 GPa, for several fixed magnetic fields up to 6 T. The non-metallic state is readily suppressed by magnetic field. At 6 T, $\text{PrFe}_4\text{P}_{12}$ has metallized and exhibits heavy fermion behavior, as evidenced by the strongly enhanced T^2 prefactor $A = 13.7 \mu\Omega\text{cm}/\text{K}^2$ which, assuming the validity of the Kadowaki-Woods relation, corresponds to a Sommerfeld coefficient of about $1 \text{ J/mol}/\text{K}^2$, in good agreement with specific heat experiments (46). From Ref. 31.

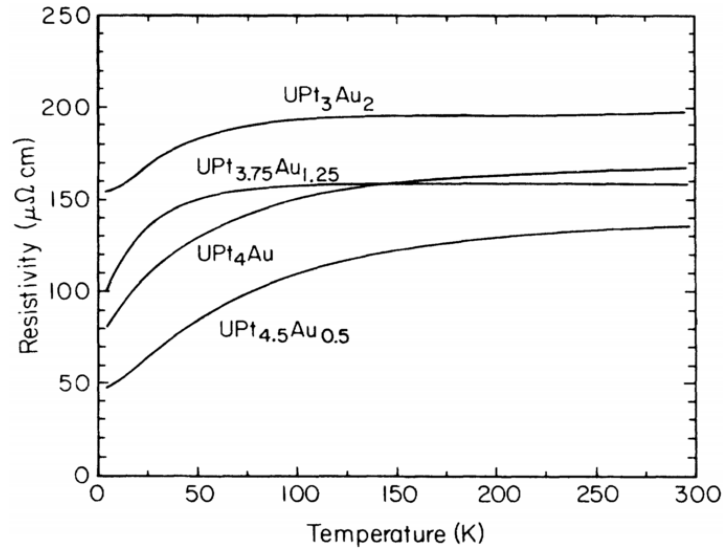


Figure S8: **Candidate two-channel Kondo material UPt₃Au₂.** (A) Temperature-dependent electrical resistivity for several UPt_{5-x}Au_x samples. The weak temperature dependence of UPt₃Au₂, together with the large resistivity values at low temperatures, suggests that it is not metallic. From Ref. 33.